

Plasma-catalytic removal of formaldehyde over Cu-Ce catalysts in a dielectric barrier discharge reactor

Xinbo Zhu^{a, b}, Xiang Gao^{a, *}, Rui Qin^a, Yuxuan Zeng^b, Ruiyang Qu^a, Chenghang Zheng^a, Xin Tu^{b, *}

^a State Key Laboratory of Clean Energy Utilization, Zhejiang University, Hangzhou, 310027, P. R. China

^b Department of Electrical Engineering and Electronics, University of Liverpool, Liverpool, L69 3GJ, UK

*Corresponding authors:

Dr. Xin Tu

Department of Electrical Engineering and Electronics,
University of Liverpool,
Liverpool, L69 3GJ, UK

E-mail: xin.tu@liv.ac.uk

Tel: +44-1517944513

*** Prof. Xiang Gao**

State Key Laboratory of Clean Energy Utilization,
Zhejiang University,
Hangzhou 310027,
China

E-mail: xgao1@zju.edu.cn

24 **Abstract**

25 In this study, a coaxial dielectric barrier discharge (DBD) reactor has been used for plasma-catalytic
26 removal of low concentration formaldehyde over a series of Cu-Ce oxide catalysts prepared by the
27 citric acid sol-gel method. The effect of the Cu/Ce molar ratio on the removal of formaldehyde and
28 CO₂ selectivity has been investigated as a function of specific energy density (SED). In comparison
29 to the plasma-only process, the combination of plasma with the Cu-Ce binary oxide catalysts
30 significantly enhances the reaction performance, while the presence of CuO or CeO₂ in the DBD
31 reactor has a negative effect on the removal of HCHO. This suggests that the interactions between
32 Cu and Ce species change the properties of the catalysts and consequently affect the performance of
33 the plasma-catalytic process. The highest removal efficiency of 94.7% and CO₂ selectivity of 97.3%
34 were achieved when the Cu₁Ce₁ catalyst (Cu/Ce = 1:1) was placed in the DBD reactor at the SED of
35 486 J L⁻¹. The interaction between Cu and Ce species results in a larger specific surface area and pore
36 volume, along with a greater formation of surface adsorbed oxygen (O_{ads}), which favor the oxidation
37 of formaldehyde in the plasma process. In addition, the redox cycles between Cu and Ce species
38 facilitate the formation of additional active oxygen atoms and contribute to the plasma-catalytic
39 oxidation reactions. Plausible reaction mechanisms involved in the plasma-catalytic oxidation of
40 HCHO have been proposed.

41 **Keywords:** Plasma-catalysis; Dielectric barrier discharge (DBD); Formaldehyde; Cu-Ce catalysts

42

43

44

45

46 **Highlight**

- 47 • Cu-Ce binary catalysts show excellent HCHO removal efficiency and CO₂ selectivity.
- 48 • Electronic excitations become more important with increasing specific energy density.
- 49 • Surface adsorbed oxygen plays an important role in plasma-catalytic reactions.
- 50 • Both gas phase and surface reactions contribute to HCHO removal.

51

52

53

54

55

56

57

58

59

60

61

62

63

64

65

66

67

68 **1. Introduction**

69 Formaldehyde (HCHO) is a hazardous air pollutant that is mainly emitted from industrial
70 processes such as the manufacturing of wood products and building materials, and combustion
71 processes. As one of the toxic volatile organic compounds (VOCs), the emission of formaldehyde has
72 become a great concern in our society due to its harmful effects on our health and environment,
73 especially as a suspected carcinogen. Significant efforts have been devoted to the development and
74 investigation of various pollution remediation technologies including adsorption, membrane
75 separation, biological process, thermal combustion and catalytic oxidation for the removal of
76 formaldehyde. However, conventional technologies are not cost-effective for the removal of low
77 concentration VOCs (e.g. formaldehyde) in high volume waste gas streams. For example, thermal
78 processes require large amounts of energy for heating the high volume gas flow to clean only a low
79 concentration of environmental pollutants.

80 Non-thermal plasma (NTP) has been regarded as a promising method for the removal of a wide
81 range of low concentration volatile organic compounds (VOCs) due to its non-equilibrium character,
82 fast reaction, low energy cost and unique ability to initiate both physical and chemical reactions at
83 low temperatures [1]. Energetic electrons generated in non-thermal plasma can collide with carrier
84 gases, forming highly reactive species such as free radicals and excited atoms, molecules and ions.
85 These species are capable of breaking most chemical bonds or initiating chemical reactions, leading
86 to the removal of various VOC pollutants [2]-[5]. However, the selectivity toward the desired final
87 products (e.g. CO₂ and H₂O) through deep oxidation is typically low when using plasma discharge
88 alone, whilst the formation of unwanted by-products is inevitable [3][5]. Recently, a hybrid plasma-
89 catalysis technology has been developed to combine the advantages of high selectivity from catalysis

90 with the low temperature, fast reaction provided by non-thermal plasma [6]-[8]. The integration of
91 plasma and catalysis has great potential to reduce the operating temperature of catalyst activation,
92 enhance the removal efficiency of the gas pollutant and increase the selectivity of the desired final
93 products to minimise the formation of unwanted by-products (such as NO_x); all of which contribute
94 to enhancing the energy efficiency of the process [8]-[10].

95 Catalysts are regarded as one of the most important factors to determine the reaction performance
96 of a plasma-catalysis system. Different catalysts including γ -Al₂O₃, TiO₂, zeolite 13X and NaNO₂
97 coated raschig rings, have been shown to enhance the process performance for the plasma-catalytic
98 oxidation of formaldehyde [11][12]. Ding et al. found that the presence of Ag/CeO₂ catalysts in a
99 dielectric barrier discharge (DBD) significantly improved the removal efficiency and CO₂ selectivity
100 of formaldehyde, which can be attributed to the formation of plasma-enhanced catalytic redox cycles
101 between Ag and Ce species [13]. Zhao et al. also reported a similar interaction effect from Ag and Cu
102 in the AgCu/HZSM-5 for formaldehyde removal in a cycled storage–discharge (CSD) system [14].
103 However, high costs of noble metals could limit the use of these catalysts for industrial applications.
104 Up until now, the knowledge of supported metal oxide catalysts, especially the binary oxide catalysts,
105 for the plasma-catalytic oxidation of formaldehyde is rather limited [15][16].

106 Cu-based catalysts have been widely used in the oxidation of VOCs due to their sufficient
107 catalytic activity and relatively low cost [17]. Cerium oxide (CeO₂) has been regarded as an effective
108 promoter in thermal catalytic reactions due to its high oxygen storage capacities and redox properties
109 between Ce⁴⁺ and Ce³⁺. CeO₂ can also act as a local source/sink of oxygen species due to its high bulk
110 oxygen mobility and oxygen vacancies [18]. Cu-Ce mixed oxides have been regarded as promising
111 catalysts for thermal catalytic oxidation of VOCs, such as benzene and toluene, due to the strong

112 interactions between Cu and Ce species [19][20]. However, the combination of Cu-Ce oxide catalysts
113 with non-thermal plasmas for the oxidation of VOCs has not yet been reported [21]. It is still not clear
114 how the interactions between Cu and Ce species will affect the plasma-catalytic oxidation process.

115 In this study, a series of Cu-Ce oxide catalysts with different molar ratios have been prepared by
116 a citric acid method. The effect of these catalysts on plasma-catalytic removal of formaldehyde as a
117 function of specific energy density (SED) has been investigated in terms of formaldehyde removal
118 efficiency and CO₂ selectivity. Catalyst characterization has been carried out using a wide range of
119 analytic techniques such as Brunauer, Emmett and Teller (BET) surface measurement, X-ray
120 diffraction (XRD) and X-ray photoelectron spectroscopy (XPS) to get a better understanding of the
121 roles of these catalysts in the plasma-catalytic process. Plausible reaction mechanisms and pathways
122 have also been proposed and discussed.

123

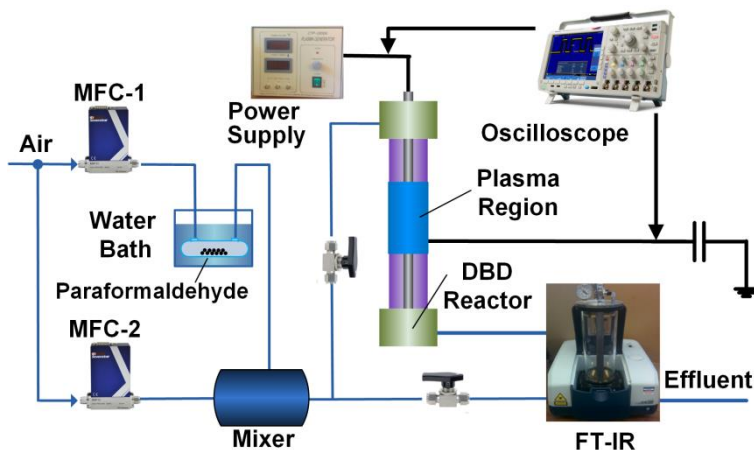
124 **2. Experimental Section**

125 **2.1 Experimental Setup**

126 Fig. 1 shows the schematic diagram of the experimental setup. A 60 mm-long aluminum foil
127 (ground electrode) was wrapped over a quartz tube with an inner diameter of 8 mm and wall thickness
128 of 1 mm. A stainless steel rod with an outer diameter of 4 mm was placed in the axis of the quartz
129 tube and acted as a high voltage electrode. As a result, the length of the discharge zone was 60 mm
130 with a discharge gap of 2 mm. Catalysts (100 mg, 35-60 mesh) were packed in the discharge region
131 and held by quartz wool, corresponding to a gas hourly space velocity (GHSV) of 600000 mL g⁻¹ h⁻¹.
132 In this study, simulated dry air was used as carrier gas. Gaseous formaldehyde was acquired by
133 feeding a dry air stream through paraformaldehyde powders (99.9%, Alfa Aesar) which were

134 contained in a vessel heated in a water bath (60 °C). The total flow rate for the experiments was fixed
 135 at 1 L min⁻¹ with a corresponding residence time of 0.23 s in the discharge area. The initial
 136 concentration of formaldehyde was kept at 57.7 ppm.

137



138

139

Fig. 1.

140

141 The DBD reactor was supplied by an AC high voltage power supply with a maximum peak
 142 voltage of 30 kV and a frequency of 10 kHz. A high voltage probe (Testec, HVP-15HF, 1000:1) was
 143 used to measure the applied voltage of the discharge, while a Tektronix P5100 probe was used to
 144 measure the voltage across the external capacitor C_{ext} (0.47 μ F). All the electrical signals were
 145 monitored by a digital oscilloscope (Tektronix 3034B). V-Q Lissajous method was used to calculate
 146 the discharge power (P) of the DBD reactor. In the present work, specific energy density has been
 147 defined as energy dissipated to the plasma per unit volume:

$$148 \quad SED \left(\frac{J}{L} \right) = \frac{P \text{ (W)}}{Q \text{ (L / min)}} \times t$$

149 where P is the discharge power and Q is the total flow rate.

150 Effluent compositions were analyzed online using a Fourier transform infra-red (FTIR)
151 spectrometer (Jasco FT/IR-4200, resolution of 2 cm^{-1}) equipped with a 1–16 m variable gas cell
152 (PIKE Technologies). The effective pathlength of the gas cell used in this study was 5.3 m.
153 Measurements were carried out after running the plasma system for about 40 minutes, when a steady-
154 state had been reached. All the signals were obtained by averaging 128 scans. Quantitative analysis
155 was carried out by comparing the obtained signals with the standard FTIR spectra from Pacific
156 Northwest National Laboratory (PNNL) database. The removal efficiency of formaldehyde is defined
157 as:

$$158 \quad \eta_{\text{HCHO}} = \frac{c_{in} - c_{out}}{c_{in}} \times 100\%$$

159 where c_{in} and c_{out} are inlet and outlet concentrations of formaldehyde, respectively.

160 The selectivity of carbon dioxide (CO_2) is defined as follows:

$$161 \quad \text{CO}_2 \text{ selectivity} (\%) = \frac{c_{\text{CO}_2}}{c_{\text{CO}} + c_{\text{CO}_2}} \times 100$$

162 where c_{CO} and c_{CO_2} are CO and CO_2 concentrations in the effluent, respectively.

163

164 2.2 Model Description

165 A Boltzmann equation solver called BOLSIG+ was used to calculate the electron energy
166 distribution in the plasma together with the energy deposition in various electron-induced collisions
167 [22][23]. Based on the classical two term approximation, BOLSIG+ provided steady solutions to the
168 Boltzmann equation in the selected range of the reduced electric field (E/N, ratio of electric field to
169 the number density of carrier gas molecules, in Td) and gave outputs of the corresponding electron
170 energy distribution function (EEDF), mean electron energy, reaction rate coefficients and energy

171 fractions of each plasma reaction channel. The reduced electric field was obtained from the
172 experimental data, while an electron number density of 10^{19} m^{-3} was chosen as the initial condition
173 for the calculation, which was within the same order of magnitude of experimental results (10^{18} – 10^{21}
174 m^{-3}) of air DBDs [24][25]. The cross section data of N_2 and O_2 used in this study was obtained from
175 Phelps [26] and Lawton [27], while the effect of formaldehyde was excluded due to its low
176 concentration (57.7 ppm) in the air flow (79% N_2 and 21% O_2). A list of chosen reactions has been
177 given in Table S1 (Supporting Information).

178

179 **2.3 Catalysts Preparation**

180 A series of Cu-Ce mixed oxides with different Cu/Ce molar ratios (1:3, 1:1 and 3:1) were
181 prepared using the citric acid method. The desired amount of copper nitrate, ceria nitrate and citric
182 acid (99.9%, Alfa Aesar) were mixed and then dissolved in deionized water. The molar ratio of citric
183 acid to metal salts was 1.5. The above solution was stirred at room temperature for 2 h, followed by
184 drying in a water bath at 80 °C. The obtained samples were heated overnight at 110 °C and then
185 calcined at 500 °C for 5 h. All the catalysts were sieved in 35-60 meshes for testing. Pure copper
186 oxide and ceria oxide were prepared using a similar procedure.

187

188 **2.4 Catalyst Characterization**

189 N_2 adsorption and desorption experiments were carried out to determine the specific surface area,
190 pore size distribution and average pore diameter of the catalysts using an Autosorb-1-C instrument
191 (Quantachrome Instrument Crop). XRD patterns of the catalyst samples were recorded by a Rigaku
192 D/max 2550PC system with a $\text{Cu-K}\alpha$ radiation in the 2θ range from 10° to 80° . X-ray photoelectron

193 spectroscopy spectra were recorded with a Thermo ESCALAB 250 using Al K α X-ray ($h\nu = 1486.6$
194 eV) at 150 W as a radiation source. Sample charging effect was eliminated by correcting the observed
195 spectra with the C 1s binding energy (B. E.) value of 284.6 eV. Carbon deposition on the surface of
196 spent catalysts was evaluated by thermogravimetric analysis (TGA) and differential thermal analysis
197 (DTA) in an air atmosphere using a Thermal MAX 500 instrument at a heating rate of 10 °C min⁻¹
198 from 20 °C to 900 °C.

199

200 **3. Results and Discussions**

201 **3.1 Catalyst properties**

202 **3.1.1 Structure of Cu-Ce catalysts**

203 The isotherms of nitrogen adsorption/desorption for all the samples are of type IV, which is
204 associated with capillary condensation in mesopores [28]. Type H3 hysteresis loops are observed
205 closing at $P/P_0 = 0.4$ for all the catalysts, which indicate typical open slit-shaped pores with parallel
206 walls and ink-bottle-shaped pores [29]. Table 1 shows the specific surface area (S_{BET}), total pore
207 volume and average pore diameter of all the fresh catalysts. A synergy resulting from the interactions
208 between Cu oxide and Ce oxide can be clearly observed. The specific surface area (33.0 – 64.4 m² g⁻¹
209 ¹) of the Cu-Ce catalysts is significantly enhanced compared to that of pure CuO (3.6 m² g⁻¹) and
210 CeO₂ (10.3 m² g⁻¹). The highest S_{BET} and total pore volume were obtained for the Cu1Ce1 catalyst,
211 while further increasing of the amount of Cu or Ce resulted in a decrease of the S_{BET} and pore volume
212 of the catalysts.

213

214

Table 1.

Sample	S_{BET} ($\text{m}^2 \text{g}^{-1}$)	Total pore volume ($\text{cm}^3 \text{g}^{-1}$)	Average pore diameter (nm)	Crystallite size ^a (nm)	Lattice constant ^b (Å)	Ce^{3+} / $\text{Ce}^{3+}+\text{Ce}^{4+}$ ^c (%)	O_{ads} / $\text{O}_{\text{ads}} + \text{O}_{\text{lat}}$ ^d (%)
CuO	3.6	0.010	8.4	25.43	-	--	-
Cu3Ce1	33.0	0.044	6.7	5.12	5.4095	19.94	34.05
Cu1Ce1	64.4	0.081	4.4	4.58	5.4097	24.54	38.22
Cu1Ce3	41.7	0.063	6.2	4.77	5.4100	14.55	36.12
CeO ₂	10.3	0.035	7.7	17.44	5.4104	9.78	26.70
Spent Cu1Ce1	60.8	0.078	4.8	4.58	5.4097	23.87	33.02

216 ^a All column data correspond to crystallite size of CeO₂ except for the first one, which corresponds
217 to CuO.

218 ^b Calculated from the characteristic peak of CeO₂ (111) crystal face located at $2\theta = 28.5^\circ$ in the XRD
219 patterns.

220 ^c Relative percentage of Ce³⁺ on catalyst surface are calculated from XPS data.

221 ^d Relative percentage of surface oxygen species (O_{ads}) are calculated from XPS data, while O_{lat} is
222 lattice oxygen species of Cu-Ce catalysts.

223

224 Fig. 2 presents the XRD patterns of the fresh and spent catalysts. For the CuO catalyst, typical
225 diffraction patterns of CuO phase (JCPDS 45-0937) can be clearly seen, while the CeO₂ and all fresh
226 Cu-Ce catalysts show a typical cubic fluorite-type oxide structure (JCPDS 34-0394). No obvious
227 reflections of a copper oxide phase are found in the Cu1Ce1 and Cu1Ce3 samples, which can be
228 attributed to the well dispersed CuO on the surface of CeO₂ [30]. Further increasing of the Cu
229 content leads to the formation of bulk CuO particles, since the characteristic peaks of CuO at $2\theta =$
230 35.5° and 38.5° are detected in the Cu3Ce1 catalyst. The diffraction peaks of all the Cu-Ce catalysts
231 are broader compared to those of CuO and CeO₂, while the peak intensities of the Cu-Ce catalysts are
232 smaller, indicating the decrease of CeO₂ crystallinity by Cu doping, which is in accordance with the
233 calculated crystalline size of CeO₂ (Table 1) using the Scherrer's equation [31]

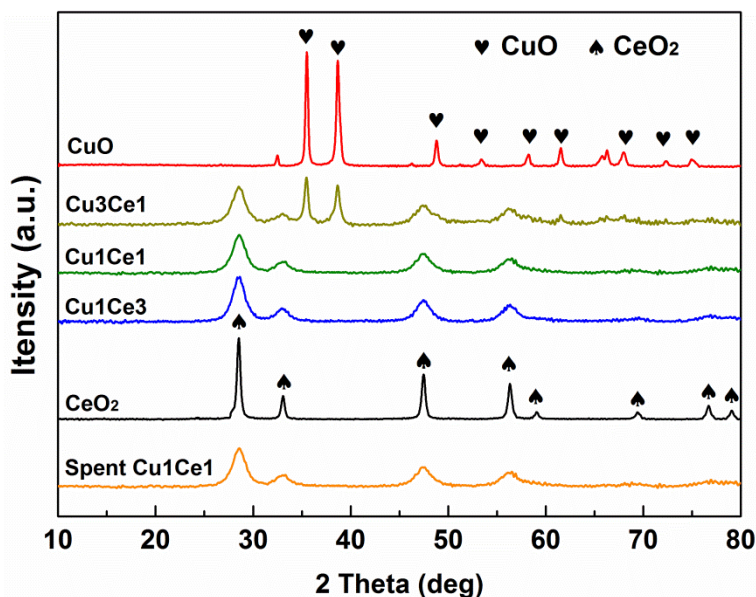
234

$$d = \frac{0.89\lambda}{(\beta - \beta_0) \cos \theta} \quad (2)$$

235 where d is the average volume diameter of the crystallite, λ is the wavelength of the incident X-rays
236 from the Cu source, θ is the X-ray incidence angle with respect to the sample surface, β is the peak
237 width at half peak height (in radians) and β_0 is the instrumental line broadening.

238 Pure CeO₂ and CuO have a crystallite size of 17.44 nm and 25.43 nm, respectively, but it
239 decreases significantly to 4.58-5.12 nm in the case of the Cu-Ce catalysts, which is in agreement with
240 the results of N₂ adsorption-desorption experiments in this study. The XRD patterns of the Cu-Ce
241 catalysts show a slight shift of about +0.3° for the characteristic peak of CeO₂ (111) crystal face
242 located at $2\theta = 28.5^\circ$. This behavior can be explained by the incorporation of CuO into the CeO₂
243 lattice and the partial substitution of Ce cations by Cu cations. Since the radius of Cu²⁺ (0.73 Å) is
244 smaller than that of Ce⁴⁺ (0.97 Å), a contraction of the CeO₂ lattice would occur when Ce⁴⁺ is replaced
245 by Cu²⁺, as confirmed by the decrease of the lattice constant in Table 1.

246



247

248

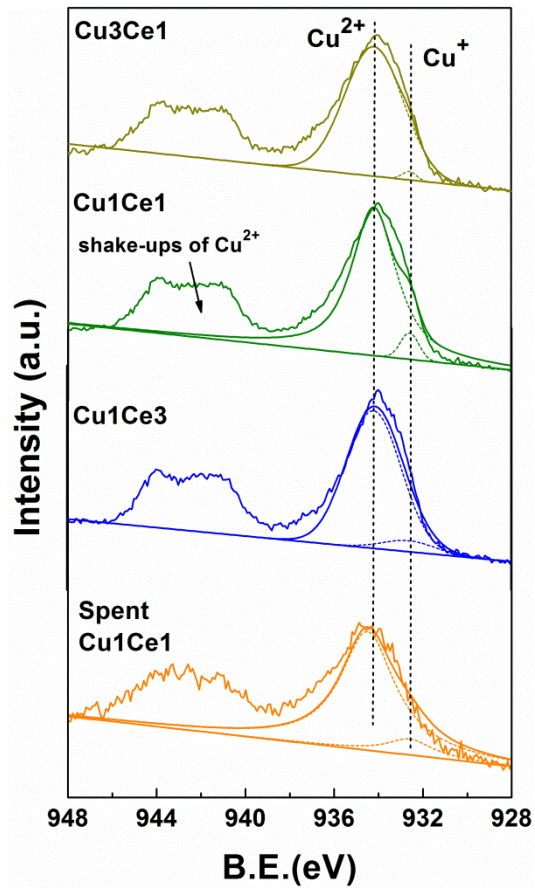
249

250 **3.1.2 Surface analysis of Cu-Ce catalysts**

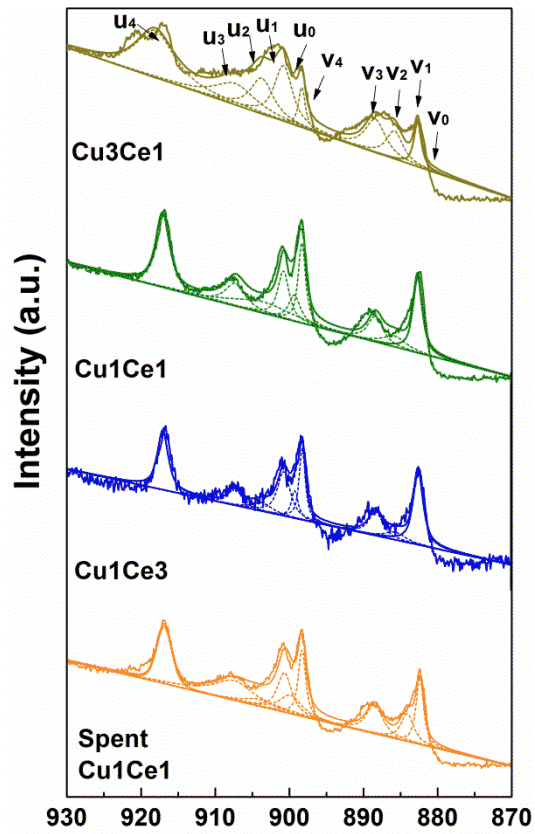
Fig. 2.

251 XPS technique has been used to gain a better insight into the chemical states of all the elements
252 on the surface of the Cu-Ce catalysts. Fig. 3 shows the XPS spectra of Cu 2p, Ce 3d and O 1s. The
253 Cu 2p (Fig. 3a) spectra show a main peak of Cu 2p_{3/2} at around 934.0 eV, along with the shake-up
254 peaks at 940-945 eV for all the Cu-Ce catalysts. The presence of the shake-up peaks and their binding
255 energy demonstrate the existence of Cu²⁺ species on the catalyst surface [32]. Deconvolution of Cu
256 2p_{3/2} shows two peaks centered at 934.2 and 932.6 eV, respectively. The former can be identified as
257 Cu²⁺ species, while the latter one belongs to a reduced Cu species (Cu⁰ or Cu⁺). It is difficult to
258 distinguish the exact chemical state of the reduced surface Cu species using XPS since the binding
259 energy of these two species is very close. However, it is believed that Cu⁺ rather than Cu⁰ exists as
260 the main reduced Cu species on the catalyst surface since these catalysts were calcined in air [33].
261 Cu⁺ species can also be formed from the substitution at the interfaces of the oxide phases due to the
262 similar radius of Cu⁺ and Ce⁴⁺ ions [30].

263 The XPS spectra of Ce 3d shows the spin-orbit splitting of Ce 3d_{5/2} and Ce 3d_{3/2}, labeled as u and
264 v, respectively (Fig. 3b). The spectra can be divided into ten peaks. The u₂, u₀, v₂ and v₀ peaks are
265 assigned to Ce³⁺, while the rest belong to Ce⁴⁺ [34]. The relative concentration of Ce³⁺/(Ce³⁺+Ce⁴⁺)
266 ranges from 14.55% to 24.54% for the Cu-Ce catalysts, which suggests that CeO₂ is the main Ce
267 species on the surface of the Cu-Ce catalysts. The XPS spectra of O 1s are shown in Fig. 3c. Two
268 components are identified by deconvoluting the main peak at around 531 eV. The peaks at 529.6 eV
269 are identified as lattice oxygen (O²⁻) (denoted as O_{lat}), while those at 531.6 eV are assigned to the
270 surface adsorbed oxygen (denoted as O_{ads}) [35]. The relative concentration of O_{ads} ranges from 34.05%
271 to 38.22% as shown in Table 1, suggesting that lattice oxygen is the most abundant oxygen species
272 on the surface of the Cu-Ce catalysts.



(a)



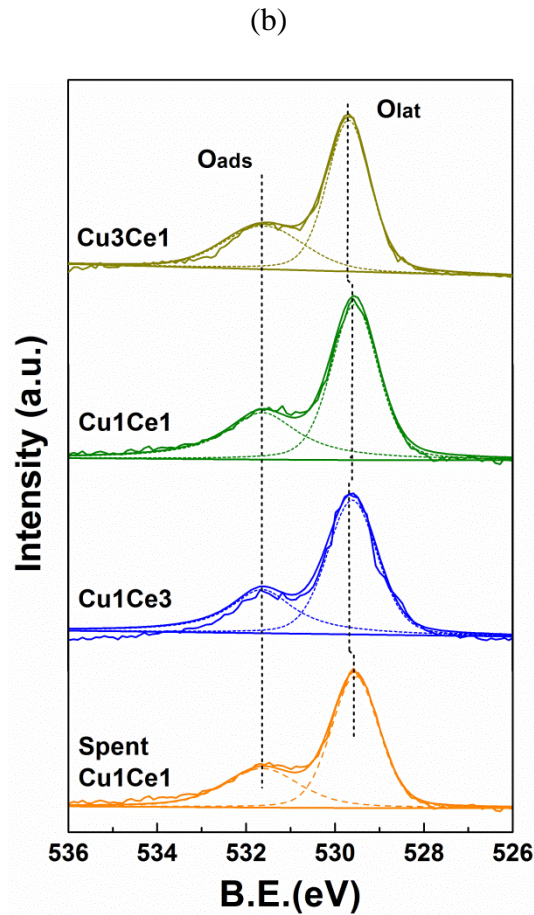


Fig. 3.

278

279

280

281

282 3.2 Plasma-catalytic removal of formaldehyde

283 Fig. 4 shows the effect of the Cu-Ce catalysts on the removal of formaldehyde as a function of

284 SED. The removal of formaldehyde increases with increasing SED regardless of the catalyst used.

285 Increasing the SED by raising the applied voltage is expected to effectively enhance the reduced

286 electric field (E/N), which changes the electron energy distribution function (EEDF) and enhances

287 the mean electron energy. This can be demonstrated by our calculation through solving the Boltzmann

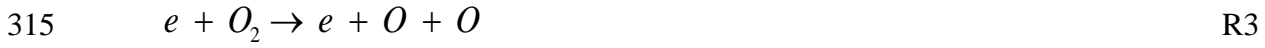
288 equation using BOLSIG+. Taking the Cu1Ce1 catalyst for example, increasing the applied voltage

289 (peak-to-peak) from 4.86 kV to 6.48 kV significantly increases the SED from 288 J L^{-1} to 486 J L^{-1} ,

290 which enhances the reduced electric field from 90 Td to 120 Td and consequently increases the mean
291 electron energy from 2.28 eV to 3.29 eV (shown in Fig. 5a). It is also found that by increasing the
292 SED, the EEDF shifts with an increase in electron density in the high-energy tail of the distribution
293 function (Fig. 5b). It is expected that increasing the SED also leads to an increase in the number of
294 microdischarges per half cycle of the applied voltage. Although it is difficult to quantify the total
295 number of microdischarges in a DBD system, previous work of Kim et al. has demonstrated through
296 the use of an intensified charge coupled device (ICCD) camera that increasing the discharge power
297 enhances the electric field, with the formation of more microdischarges in the plasma [36]. Snoeckx
298 et al. has simulated the process of plasma-based dry reforming and found the number of micro-
299 discharge pulses per half cycle has a great influence on the electron density, which in turn affects the
300 calculated conversion and selectivity of the plasma process [25]. As a result of the combined effects
301 induced by the increase of the SED, more chemically active species can be generated in the discharge
302 via electron impacts to drive the plasma chemical reactions.

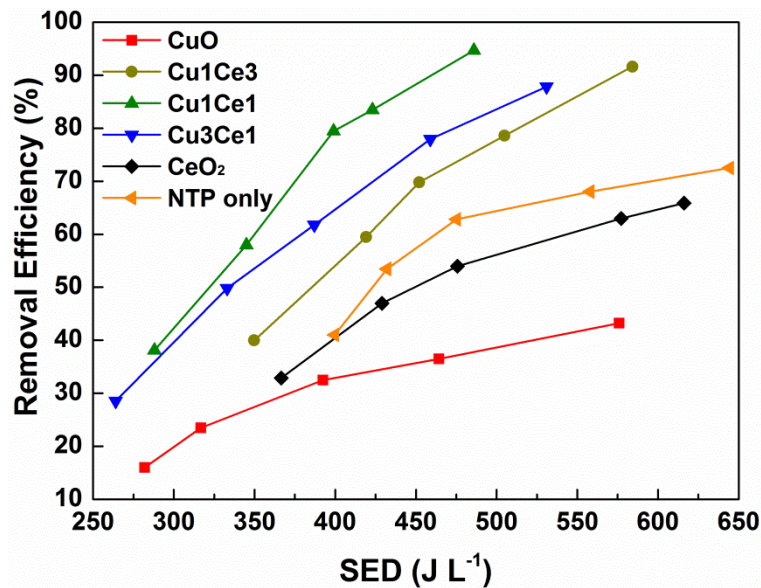
303 To get a better understanding of the initial steps of plasma chemistry, the effect of the reduced
304 electric field on the fraction of energy transferred to different electron-molecule collision channels
305 (e.g. elastic, rotational and vibrational excitations, electronic excitations and ionization) has been
306 investigated (shown in Fig. 5c). In the E/N range of 90 Td to 120 Td, the discharge energy is mainly
307 consumed by electronic, rotational and vibrational excitations. Electronic excitations become more
308 important with increasing E/N as its energy fraction increases from 31.0 to 53.6%. Meanwhile, the
309 discharge power consumed by the rotational and vibrational excitation channels is decreased from
310 68.6% to 45.6%. Only ~2.5% and ~0.3% of the energy contributes to the minor channels of elastic
311 and ionization reactions, respectively. Electronic excitation reactions contribute to the generation of

312 N and O radicals and metastable N_2 via R1-R4 [24]:



317 where $N_2(a')$ denotes the sum of N_2 metastable state of $N_2(a^1\Sigma)$, $N_2(a^1\Pi)$ and $N_2(w^1\Delta)$.

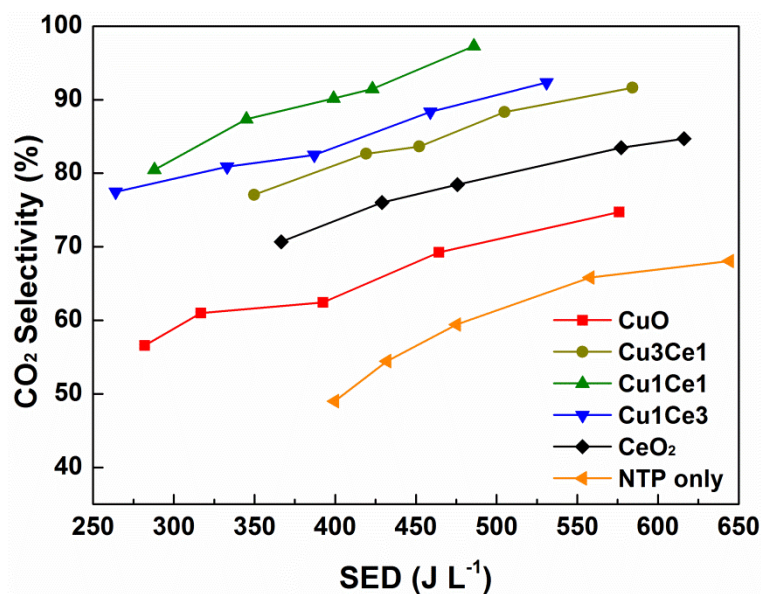
318



319

320

(a)



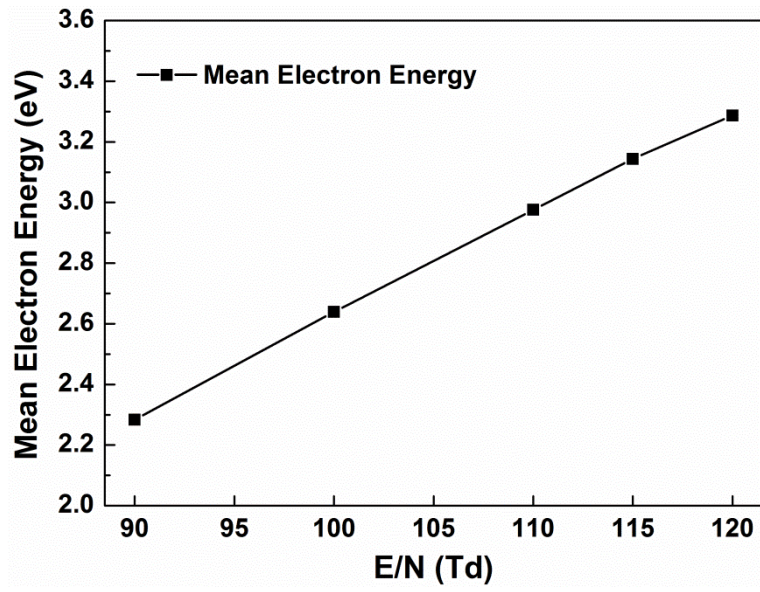
321

322

(b)

323

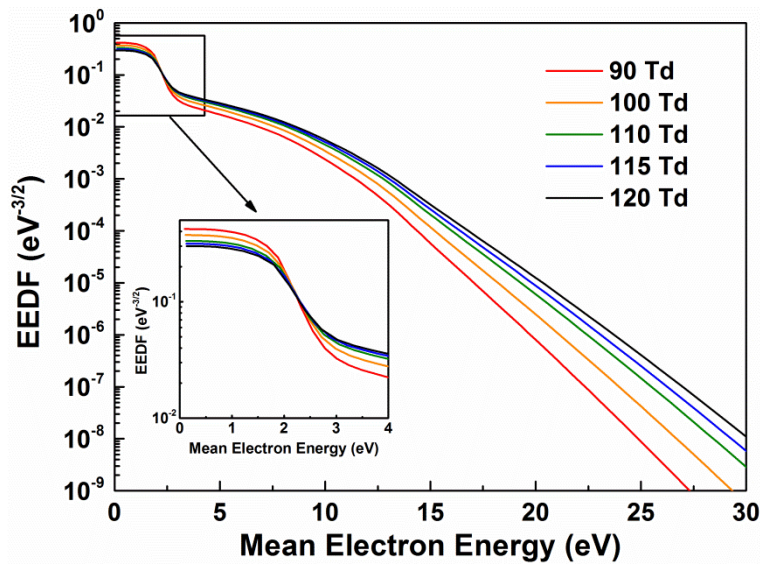
Fig. 4.



324

325

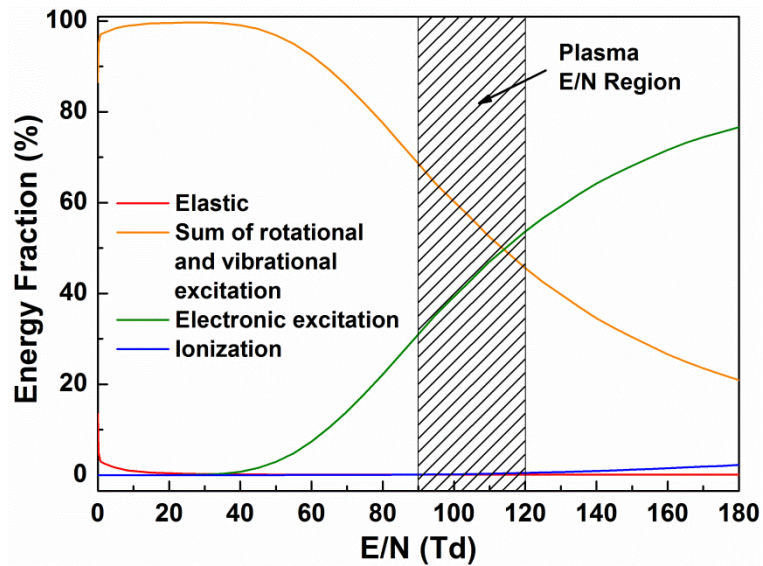
(a)



326

327

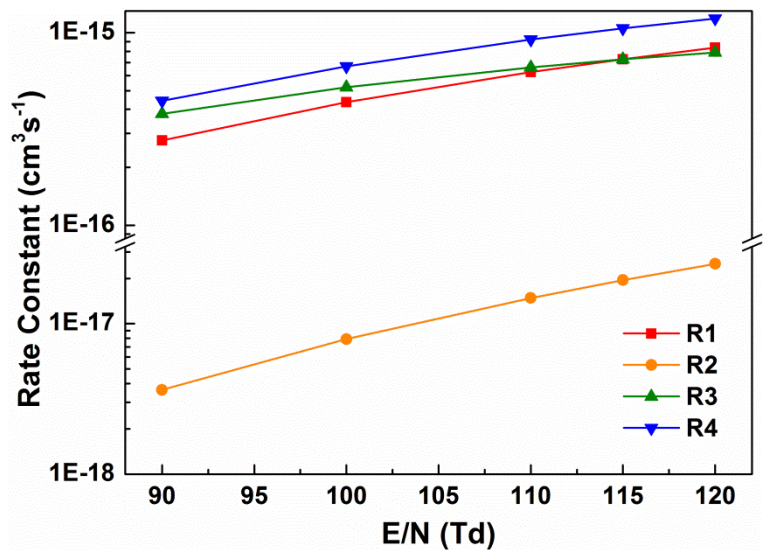
(b)



328

329

(c)



330

331

(d)

332

Fig. 5.

333

334

335

336

337

338

As shown in Fig. 5d, the rate coefficient of the reactions R1-R4 is enhanced with the increase in SED, resulting in the formation of more reactive species. The reactive species with sufficient energy could collide and react with pollutant molecules. The rotational and vibrational excited N_2 and O_2 with insufficient energy are not able to rupture the pollutant molecules, but O_2 species may play a role in the oxidation of the intermediates to CO_2 and H_2O [24].

339 Compared to the plasma process with no catalyst, the combination of plasma with the Cu-Ce
340 binary catalysts significantly enhances the removal efficiency of HCHO, while the presence of CuO
341 or CeO₂ in the DBD reactor has a negative effect on the removal of HCHO. In addition, all the catalyst
342 samples show an enhanced CO₂ selectivity when combined with the plasma. The highest
343 formaldehyde removal efficiency (94.7%) and CO₂ selectivity (97.3%) were achieved using the
344 Cu₁Ce₁ catalyst at the SED of 486 J L⁻¹, as shown in Fig. 4. These results suggest that the interactions
345 between Cu and Ce species could change the properties of the catalysts, and consequently enhance
346 the performance of the plasma-catalytic oxidation of formaldehyde. As shown in Table 1, the Cu-Ce
347 catalysts have a larger specific surface area and pore volume compared to the pure CuO and CeO₂
348 samples. It is generally recognized that adsorption is the initial step of heterogeneous catalysis. Higher
349 adsorption capacity is expected for the Cu-Ce catalysts due to their larger specific surface area which
350 can provide more adsorption sites and prolong the retention time of formaldehyde in the plasma due
351 to the diffusion of pollutants within the pores. In a single-stage plasma-catalysis system where the
352 catalyst is directly in contact with the plasma, reactive species can also be generated in the pores of
353 the catalysts, thus the probability of reactions between the adsorbed pollutant molecules and reactive
354 species in the plasma-catalysis system is enhanced [37]. Guaitella et al. found that the adsorption of
355 C₂H₂ and active species increased with increasing catalyst porosity, which led to a higher oxidation
356 of C₂H₂ in the plasma-catalytic reactions [38]. These results are in good agreement with the findings
357 of this work as the specific surface areas and pore volumes follow the same order as the removal
358 efficiency and CO₂ selectivity: Cu₁Ce₁ > Cu₁Ce₃ > Cu₃Ce₁. It is worth noting that high removal
359 efficiency of 92.9% and CO₂ selectivity of 96.4% are achieved in the plasma-catalytic removal of
360 HCHO over the Cu₁Ce₁ catalyst at a SED of 486 J L⁻¹ after reaction for 5 h, showing the satisfied

361 activity and stability of the Cu1Ce1 catalyst under the experimental conditions. The carbon deposition
362 (calculated from the TGA curve) on the spent Cu1Ce1 catalyst after 5 h reaction at the SED of 486 J
363 L⁻¹ was 0.15%. This weak coke formation could be the reason for the slightly decreased removal
364 efficiency and CO₂ selectivity. The specific surface area and pore volume of the Cu1Ce1 catalyst was
365 found to have weakly decreased after the reaction, while the average pore diameter of the catalyst
366 was slightly increased, as shown in Table 1. These changes could be attributed to the block of micro-
367 pores on the Cu1Ce1 catalyst by the carbon deposition. The XRD pattern of the spent Cu1Ce1 catalyst
368 (Fig. 2) shows no significant differences compared to that of the fresh catalyst, indicating the
369 crystallite structure of the catalyst is not changed by the plasma treatment [39].

370 Previous studies reported the formation of oxygen vacancies on the surface of Cu-Ce catalysts
371 [40][41]. It is believed that the oxygen vacancies act as adsorption–desorption centers for gas phase
372 oxygen species, which favors the generation of surface adsorbed oxygen species (O_{ads}) on the Cu-Ce
373 catalysts for the oxidation of formaldehyde [42]. The presence of Ce³⁺ on the surface of the Cu-Ce
374 catalysts confirms the formation of oxygen vacancies. The relative concentration of Ce³⁺ in the Cu-
375 Ce catalysts is found to be much higher than that of pure CeO₂ (9.78%), while the Cu1Ce1 catalyst
376 shows the highest Ce³⁺ concentration, which perfectly matches the reaction performance of the
377 plasma-catalytic process. Note that the partial substitution of Ce⁴⁺ by Cu²⁺ could also lead to the
378 formation of oxygen vacancies or the reduction of Ce⁴⁺ to Ce³⁺ to retain charge balance [43]. The
379 relative concentration of Ce³⁺ in the spent Cu1Ce1 catalyst is slightly less (23.87%) than that of the
380 fresh catalyst (24.54%), indicating that part of the Ce³⁺ are oxidized to Ce⁴⁺ during the plasma-
381 catalytic process [44].

382 Moreover, the Cu-O and Ce-O chemical bonds can be weakened in the Cu-Ce catalysts due to

383 the electron effect to form more reactive oxygen species and enhance their mobility. As confirmed by
384 XPS results of O 1s, the relative concentration of the surface adsorbed oxygen species O_{ads} in the Cu-
385 Ce samples was higher than that of pure CeO_2 , whilst the highest O_{ads} concentration of 38.22% was
386 observed in the fresh Cu1Ce1 catalyst with the best reaction performance. The concentration of O_{ads}
387 decreased to 33.02% after the plasma reaction of 5 h, which indicates that the surface adsorbed oxygen
388 species play an important role in the oxidation of formaldehyde on the catalyst surface. The presence
389 of a higher concentration of O_{ads} tends to generate more active oxygen species, which could result in
390 high removal efficiency via surface reactions [41]. A perfect correlation between the reaction
391 performance and the O_{ads} concentration for different catalysts is observed in this work.

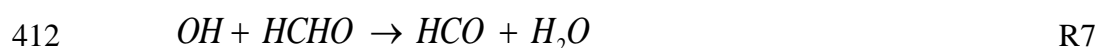
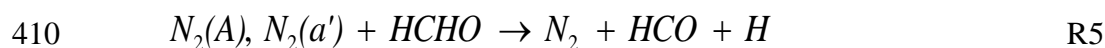
392 The redox properties of the catalysts generated from the interactions between Cu and Ce species
393 play an important role in the oxidation reactions. Previous studies showed that the redox pairs of
394 Cu^{2+}/Cu^+ and Ce^{4+}/Ce^{3+} were involved in the electron transfer process from Ce^{4+} to Cu^{2+} within the
395 $Cu^{2+}-O-Ce^{4+}$ connections in the Cu-Ce catalysts. The $Cu^{2+}-O-Ce^{4+}$ connections could bridge the
396 oxygen transfer within the structure and reduce the redox potential of the Cu species, which ensures
397 the improvement of reducibility for both Cu and Ce oxides in the Cu-Ce samples for the plasma-
398 catalytic oxidation reactions [45].

399

400 **3.3 Reaction mechanisms**

401 The main gaseous products from the plasma-catalytic reactions were CO, CO_2 and H_2O , while
402 minor products such as HCOOH were also observed. Ozone was not detected for any of the catalysts,
403 which might be decomposed due to heating or catalytic decomposition, or consumed in the plasma
404 oxidation process [46]. In this work, the removal of low concentration formaldehyde in the plasma-

405 catalysis system can be attributed to both plasma gas phase reactions and plasma-assisted surface
406 reactions on the catalyst surface. The gas phase reactions for the removal of formaldehyde are mainly
407 induced by plasma generated reactive species such as O, O(1D), OH, N and metastable N₂, as shown
408 in R5-R7 [47], while the direct electron-impact collisions only weakly affect the reaction due to the
409 low concentration of formaldehyde in the carrier gas.



413 As shown in R5-R7, HCO is the main intermediate from the initial steps of HCHO oxidation.
414 HCO species can be further oxidized by reactive species such as O and O(1D) to form end-products
415 CO, CO₂ and H₂O [13]. HCOOH is a common byproduct in plasma processing of HCHO [16].
416 HCOOH may also be formed from the oxidation of HCHO by O and O(1D) (R8) or the recombination
417 of HCO with OH (R9):

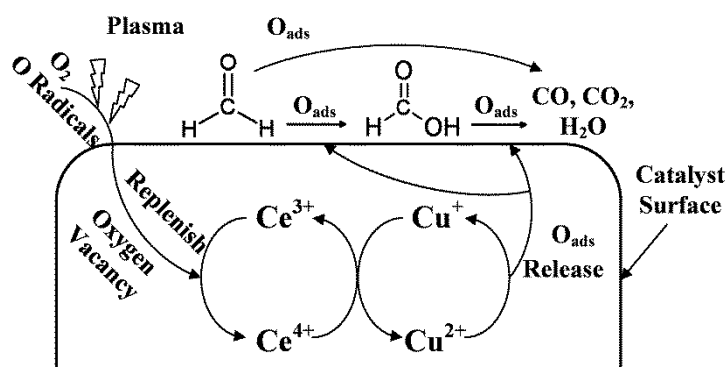


420 Plasma-assisted surface reactions also contribute to the oxidation of HCHO, while thermal
421 catalytic activation of HCHO can be ignored due to the relatively low temperature plasma process (<
422 100 °C) used in this study. In this single-stage plasma catalysis system where the Cu-Ce catalysts
423 are directly in contact with the discharge, both HCHO and intermediates from the gas phase reactions
424 can be adsorbed onto the catalyst surfaces. Short-lived active species (e.g. O) generated close to or
425 on the catalyst surface can participate in the surface reactions. It was reported that the adsorption-
426 desorption equilibrium can be significantly influenced by plasma [48]. Vibrational excited species

427 generated in plasma may also promote the adsorption of pollutants onto the catalyst surface at low
 428 temperatures [49]. The enhanced adsorption process increases the collision possibility of pollutants
 429 and active species, leading to an acceleration of the plasma chemical reactions. The adsorbed species
 430 could also react with adjacent reactive oxygen species from oxygen vacancies or gas-phase O atoms,
 431 forming intermediates such as HCO and HCOOH, before finally being oxidized to end-products such
 432 as CO₂ and H₂O. Meanwhile, Cu²⁺ sites on the catalyst surface could be reduced to Cu⁺ and re-
 433 oxidized to Cu²⁺ by the adsorbed oxygen or the lattice oxygen from CeO₂, which suggests Ce⁴⁺ acts
 434 as an oxygen source for the oxidation of HCHO [50]. The consumed oxygen species on the catalysts
 435 can be replenished by capturing oxygen molecules and reactive oxygen species generated in the
 436 plasma. The fast redox between Ce⁴⁺ and Ce³⁺ determines the oxygen storage capacity, which is
 437 important for the formation of surface oxygen species. Both Cu and Ce are able to shift between
 438 various oxidation states, while the interaction between Cu and Ce plays a significant role to enclose
 439 the redox reaction cycle, which determines the catalytic performance [45]:



441 The plausible reaction mechanisms in the plasma-assisted surface oxidation of HCHO are presented
 442 in Fig. 6:



443
444 **Fig. 6.**
445

446 **4. Conclusions**

447 In this study, the effects of the Cu-Ce catalysts and SED on the plasma-catalytic removal of
448 formaldehyde have been investigated in terms of the removal efficiency and CO₂ selectivity.
449 Compared to the plasma process in the absence of a catalyst, the presence of CuO or CeO₂ catalyst in
450 the plasma decreases the removal efficiency of HCHO, while the combination of plasma with the Cu-
451 Ce binary metal oxide catalysts significantly enhances the reaction performance regardless of the
452 SED. This can be ascribed to the interactions between Cu and Ce species over the catalyst surface.
453 The Cu₁Ce₁ catalyst (Cu/Ce=1:1) shows the best reaction performance among all the catalysts with
454 the highest removal efficiency of 94.7% and CO₂ selectivity of 97.3% at the SED of 486 J L⁻¹. The
455 combination of Cu and Ce oxides results in larger specific surface area and characteristic pore volume
456 and smaller crystalline size, all of which contribute to the plasma-catalytic oxidation of formaldehyde.
457 The interactions between Cu and Ce oxides also increase the formation of surface adsorbed oxygen
458 species and facilitate the redox cycles between Cu and Ce species, which plays a key role in the
459 plasma-induced surface reactions and significantly improves the removal efficiency of formaldehyde.
460 In this work, the removal of low concentration formaldehyde in the plasma-catalytic process can be
461 attributed to both plasma gas phase reactions and plasma-assisted surface reactions on the catalyst
462 surface.

463

464 **Acknowledgements**

465 Support of this work by the Royal Society of the UK (RG120591), the National Natural Science
466 Foundation of China (No. 51076140 & No. 51206143) and the National Science Fund for
467 Distinguished Young Scholars (No. 51125025) is gratefully acknowledged.

468

469 **References**

470 [1] H.L. Chen, H.M. Lee, S.H. Chen, M.B. Chang, *Ind. Eng. Chem. Res.* 47 (2008) 2122-2130.

471 [2] H.H. Kim, *Plasma Process. Polymers* 1 (2004) 91-110.

472 [3] R. Aerts, X. Tu, W. Van Gaens, J.C. Whitehead, A. Bogaerts, *Environ. Sci. Technol.* 47 (2013)

473 6478-6485.

474 [4] X. Tu, H. J. Gallon, J. C. Whitehead, *J. Phys. D: Appl. Phys.* 44 (2011) 482003.

475 [5] R. Aerts, X. Tu, C. De Bie, J. C. Whitehead, A. Bogaerts, *Plasma Process. Polymers* 9 (2012)

476 994-1000.

477 [6] J. Van Durme, J. Dewulf, C. Leys, H. Van Langenhove, *Appl. Catal. B: Environ.* 78 (2008) 324-

478 333.

479 [7] E. C. Neyts, A. Bogaerts, *J. Phys. D: Appl. Phys.* 47 (2014) 224010.

480 [8] J. C. Whitehead, *Pure Appl. Chem.* 82 (2010) 1329-1336.

481 [9] X. Tu, J.C. Whitehead, *Appl. Catal. B: Environ.* 125 (2012) 439-448.

482 [10] X. Tu, H. J. Gallon, M. V. Twigg, P. A. Gorry, J. C. Whitehead, *J. Phys. D: Appl. Phys.* 44 (2011)

483 274007.

484 [11] K. Hensel, Z. Machala, A. Mizuno, 2nd International Workshop on Cold Atmospheric Pressure

485 Plasmas: Sources and Applications, 85-88, Bruges, Belgium, 2005.

486 [12] W.J. Liang, J. Li, J.X. Li, T. Zhu, Y.Q. Jin, *J. Hazad. Mater.* 175 (2010) 1090-1095.

487 [13] H.X. Ding, A.M. Zhu, F.G. Lu, Y. Xu, J. Zhang, X.F. Yang, *J. Phys. D: Appl. Phys.* 39 (2006)

488 3603-3608.

- 489 [14]D.Z. Zhao, X.S. Li, C. Shi, H.Y. Fan, A.M. Zhu, *Chem. Eng. Sci.* 66 (2011) 3922-3929.
- 490 [15]Y. Wan, X. Fan, T. Zhu, *Chem. Eng. J.* 171 (2011) 314-319.
- 491 [16]X. Fan, T. Zhu, Y. Sun, X. Yan, *J. Hazard. Mater.* 196 (2011) 380-385.
- 492 [17]H.L. Tidahy, S. Siffert, F. Wyrwalski, J.F. Lamonier, A. Aboukais, *Catal. Today* 119 (2007) 317-
493 320.
- 494 [18]R. Qu, X. Gao, K. Cen, J. Li, *Appl. Catal. B: Environ.* 142-143 (2013) 290-297.
- 495 [19]S.M. Saqer, D.I. Kondarides, X.E. Verykios, *Appl. Catal. B: Environ.* 103 (2011) 275-286.
- 496 [20]C. Hu, *Chem. Eng. J.* 168 (2011) 1185-1192.
- 497 [21]H.J. Li, X.Y. Jiang, X.M. Zheng, *Appl. Surface Sci.* 280 (2013) 273-281.
- 498 [22]G.J.M. Hagelaar, L.C. Pitchford, *Plasma Sources Sci. Technol.* 14 (2005) 722-733.
- 499 [23]S. Pancheshnyi, S. Biagi, M.C. Bordage, G.J.M. Hagelaar, W.L. Morgan, A.V. Phelps, L.C.
500 Pitchford, *Chem. Phys.* 398 (2012) 148-153.
- 501 [24]A. Fridman, *Plasma chemistry*, Cambridge University Press, 2008.
- 502 [25]R. Snoeckx, R. Aerts, X. Tu, A. Bogaerts, *J. Phys. Chem. C* 117 (2013) 4957-4970.
- 503 [26]A.V. Phelps, L.C. Pitchford, *Phys. Rev. A* 31 (1985) 2932-2949.
- 504 [27]S.A. Lawton, A.V. Phelps, *J. Chem. Phys.* 69 (1978) 1055.
- 505 [28]B.C. Lippens, J. De Boer, *J. Catal.* 4 (1965) 319-323.
- 506 [29]K.S. Sing, *Pure Appl. Chem.* 57 (1985) 603-619.
- 507 [30]G. Avgouropoulos, T. Ioannides, H. Matralis, *Appl. Catal. B: Environ.* 56 (2005) 87-93.

- 508 [31]X. Tu, H. J. Gallon, J. C. Whitehead, *Catal. Today* 211 (2013) 120-125.
- 509 [32]D. Mrabet, A. Abassi, R. Cherizol, T.-O. Do, *Appl. Catal. A: General* 447 (2012) 60-66.
- 510 [33]W. Liu, M. Flytzani-Stephanopoulos, *J. Catal.* 153 (1995) 317-332.
- 511 [34]M. Skoda, M. Cabala, I. Matolinova, T. Skala, K. Veltruska, V. Matolin, *Vacuum* 84 (2009) 8-
512 12.
- 513 [35]J.C. Dupin, D. Gonbeau, P. Vinatier, A. Levasseur, *Phys. Chem. Chem. Phys.* 2 (2000) 1319-
514 1324.
- 515 [36]H.H. Kim, A. Ogata, *Eur. Phys. J. Appl. Phys.* 55 (2011) 13806.
- 516 [37]F. Holzer, *Appl. Catal. B: Environ.* 38 (2002) 163-181.
- 517 [38]O. Guaitella, F. Thevenet, E. Puzenat, C. Guillard, A. Rousseau, *Appl. Catal. B: Environ.* 80
518 (2008) 296-305.
- 519 [39]X. Tang, K. Li, H. Yi, P. Ning, Y. Xiang, J. Wang, C. Wang, *J. Phys. Chem. C* 116 (2012)
520 10017-10028.
- 521 [40]G. Marbán, A.B. Fuertes, *Appl. Catal. B: Environ.* 57 (2005) 43-53.
- 522 [41]G. Zhou, H. Lan, T. Gao, H. Xie, *Chem. Eng. J.* 246 (2014) 53-63.
- 523 [42]M. Roxana Morales, F.N. Agueero, L.E. Cadus, *Catal. Lett.* 143 (2013) 1003-1011.
- 524 [43]A. Martinezarias, D. Gamarra, M. Fernandezgarcia, X. Wang, J. Hanson, J. Rodriguez, *J. Catal.*
525 240 (2006) 1-7.
- 526 [44]W. Shan, M. Fleys, F. Lopicque, D. Swierczynski, A. Kiennemann, Y. Simon, P.-M. Marquaire,
527 *Appl. Catal. A: General* 311 (2006) 24-33.

- 528 [45]U. Menon, H. Poelman, V. Bliznuk, V.V. Galvita, D. Poelman, G.B. Marin, J. Catal. 295 (2012)
529 91-103.
- 530 [46]F. Holzer, F.D. Kopinke, U. Roland, Plasma Chem. Plasma Process.25 (2005) 595-611.
- 531 [47]N. Blin-Simiand, S. Pasquiers, F. Jorand, C. Postel, J.R. Vacher, J. Phys. D: Appl. Phys. 42
532 (2009) 122003.
- 533 [48]N. Blin-Simiand, P. Tardiveau, A. Risacher, F. Jorand, S. Pasquiers, Plasma Process. Polymers 2
534 (2005) 256-262.
- 535 [49]T. Nozaki, H. Tsukijihara, W. Fukui, K. Okazaki, Energy & Fuels 21 (2007) 2525-2530.
- 536 [50]C. He, Y. Yu, C. Chen, L. Yue, N. Qiao, Q. Shen, J. Chen, Z. Hao, RSC Advances 3 (2013) 19639.

537

538

539

540

541

542 **Figure captions**

543 Fig. 1. Schematic diagram of the experimental setup.

544 Fig. 2. XRD patterns of fresh and spent catalysts.

545 Fig. 3. XPS spectra of fresh and spent Cu-Ce binary catalysts (a) Cu 2p; (b) Ce 3d; (c) O 1s.

546 Fig. 4. Effect of different catalysts on (a) removal efficiency of formaldehyde; (b) CO₂ selectivity as

547 a function of SED.

548 Fig. 5. (a) Calculated mean electron energy; (b) EEDF; (c) energy fraction consumed in different
549 electron impact reactions; (d) rate constants of reactions for the formation of N and O radicals in the
550 plasma-catalysis system over the Cu₁Ce₁ catalyst (E/N: 90 - 120 Td; SED: 288-486 J L⁻¹).

551 Fig. 6. Plausible reaction mechanisms on catalyst surface.

552

553 **Table Captions**

554 Table. 1. Physicochemical characteristics of the catalysts.

555

556

557